



HAL
open science

Assessments of High-Power Solid State Transformers based on Grain-Oriented magnetic cores

Houssam Ichou, Mathieu Rossi, Daniel Roger, Thierry Belgrand

► **To cite this version:**

Houssam Ichou, Mathieu Rossi, Daniel Roger, Thierry Belgrand. Assessments of High-Power Solid State Transformers based on Grain-Oriented magnetic cores. IEEE International Symposium on Diagnostics for Electric Machines, Power Electronics and Drives (SDEMPED), Aug 2019, Toulouse, France. hal-04287818

HAL Id: hal-04287818

<https://hal.science/hal-04287818>

Submitted on 15 Nov 2023

HAL is a multi-disciplinary open access archive for the deposit and dissemination of scientific research documents, whether they are published or not. The documents may come from teaching and research institutions in France or abroad, or from public or private research centers.

L'archive ouverte pluridisciplinaire **HAL**, est destinée au dépôt et à la diffusion de documents scientifiques de niveau recherche, publiés ou non, émanant des établissements d'enseignement et de recherche français ou étrangers, des laboratoires publics ou privés.

Assessments of High-Power Solid State Transformers based on Grain-Oriented magnetic cores

H. Ichou, D. Roger, Senior Member, IEEE, M. Rossi, T. Belgrand

Abstract—All fields of activity using electric energy are more than ever challenged for efficiency and versatility of energy flow at reasonable costs. The emergence of electronic components with high voltage and current capabilities enables to cope with those challenges. The paper deals with assessments on Medium Frequency (MF) high-power Solid State Transformer (SST). A good technical-economic balance can be achieved by assembling suitable high power SST cells made with mature technologies for power electronics, magnetic cores and simple and reliable control strategies. In this framework, the study and design of a SST based on elementary cells involving a Grain Oriented Electrical Steel (GOES) core is addressed.

Index Terms—Grain Oriented Electrical Steel, Medium Frequency Transformer, Solid-State Transformer (SST).

I. INTRODUCTION

SOLID State transformers (SST) are getting more and more popular due to increased ability of semi-conductor components to switch high voltages and currents as well as in the development of strategies for controlling the reversible power flow in electric grids. This growing technology, already used for HVDC [1], is promising for smart grids development [2] but also for shrinking down the size of the components of grid nodes. The grid stability need nodes able to control the energy flow, which makes key assets the SSTs. It may also be used to reduce the volumes of converters for e-mobility, railway traction, substations or marine applications [3] [4].

The transformer is a critical element to the SST-cell, in that it enables the voltage change as well as the galvanic separation between input and output converters. Many research works have been performed on SST involving transformers based on amorphous or nanocrystalline magnetic cores [5] [6]. In these latter cases, power converters are requiring high level technologies and complex topologies [5] [6].

Small size SST means high frequency and high flux density level in magnetic cores. Multilevel topologies are of growing interest [7] [8] [9], because they are more prone to reproduce the classical sinusoidal case and are build to avoid strong dV/dt 's adverse effects. Conversely the use of two or three levels rectangular wave-forms is far more simple for high-power applications. A methodology for analyzing the overall losses of medium frequency transformers in a SST cell supplied by non-sinusoidal voltages have been studied in [10]. Several

approach of losses estimation can be used, such as the Improved Generalized Steinmetz Equation (IGSE) [11].

The paper analyses the possibilities for designing high-power SST cells made with well experienced components. The transformer is built around a wound core made of thin Grain Oriented Electrical Steel (GOES) sheets adapted to medium frequencies (MF) and high peak flux density. GOES are mature products, available on the market and offering widths up to 1m, high saturation levels (2.03T) and high temperature capabilities (up to 400 °C without major loss of its magnetizing ability) thanks to its mineral insulation layers. Shaped into a wound core, the electrical steel is then used such as the magnetization process occurs parallel to the easy Rolling Direction magnetization axis; avoiding any extra losses due to corners of a stacked structure.

The proposed assessments consider both the SST cell structure and the transformer properties. The cooling system design is out of the scope of the paper.

II. SOLID STATE TRANSFORMERS CELL

A. SST cell structure

The basic concept of the cell is shown in Fig.1. The SST cell consists of a Medium-Frequency Transformer (MFT) and two single phase converters. The power transfer P of a MFT depends on its volume, on frequency f , on flux density B_m and on thermal balance [12].

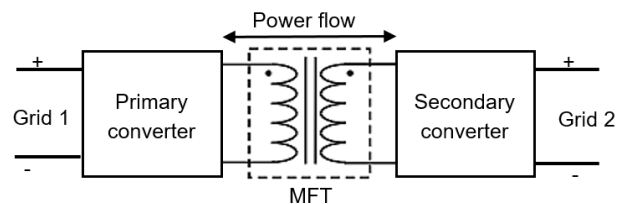


Fig. 1: Topology of a SST cell based on a simple MFT.

The maximum power flow in the MFT is given by (1), where the core cross-section A_e and the winding area A_w corresponds to the MFT volume [12]. K_B is window filling factor, K_i is the crest factor, and J the current density in the conductor, which depends on the global thermal balance.

$$P = K_i \cdot K_B \cdot J \cdot A_e \cdot A_w \cdot f \cdot B_m \quad (1)$$

From (1), the size of the transformer can be expressed as a function of frequency and peak flux density :

$$A_e \cdot A_w = \frac{P}{f \cdot B_m \cdot K_i \cdot K_B \cdot J} \quad (2)$$

The decrease of the MFT size is obtained by increasing the frequency or/and by increasing the peak magnetic induction level. This has a strong influence on specific loss [13] and consequently a good balance between all the parameters has to be found.

When combined together to transfer higher power values, the SST cells are connected in series to the High Voltage (HV) grid and in parallel on Low voltage (LV) one. The converters connected in series are placed in side insulated racks, control signals are transferred via optic fiber that ensure common-mode insulation. The MFT primary winding common-mode insulation level must be reinforced compared to the secondary one connected to the LV grid. Fig. 2 shows the MFT topology.

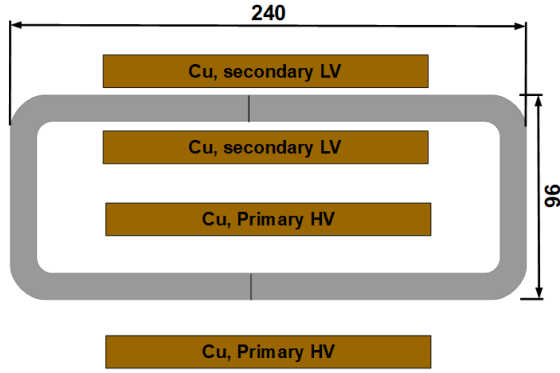


Fig. 2: Core and windings of the MFT with distances able to withstand 30kV for the primary coil common-mode insulation.

B. Estimation of losses in the converters

The details of the SST cell are presented in Fig.3 where each IGBT leg operates only one switching per period imposing rectangular voltages v_1 and v_2 . The voltage and current wave-forms are shown in Fig. 4. The time shift of v_2 relatively to v_1 controls the power flow. Fig. 4 is drawn for a time shift that corresponds to the maximum power flow from grid 1 toward grid 2.

The MFT voltage ratio is set to 1 and the two dc grid voltage levels are supposed to have their amplitudes equal to each other ($v_A = v_B$). For the core size defined in Fig. 2, the magnetizing current is much lower than the load current, corresponding to the energy transfer from a grid to the other, because of the very high magnetic permeability of the wound GOES core. The peak

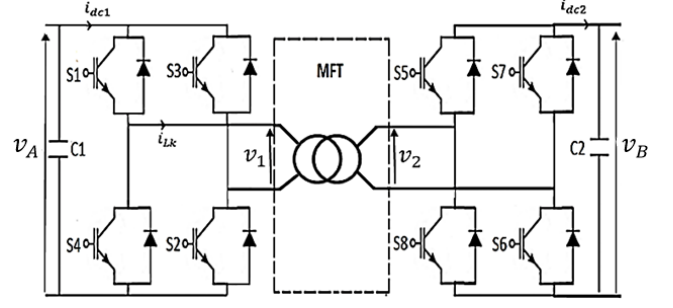


Fig. 3: SST structure of an elementary cell.

magnetizing current in less than 0.5A for every configurations considered in section E that correspond to peak load current in the range of 80A – 100A.

As the magnetizing current can be neglected in a first approach, the current waveform depends on the instantaneous voltage difference $v_1 - v_2$ and on the leakage inductance L_K of the MFT when the resistances are neglected.

$$L_K \frac{di_{LK}}{dt} = v_1 - v_2 \quad (3)$$

The second graph of Fig. 4 shows the voltage difference ($v_1 - v_2$) and the resulting current i_{LK} flowing across the windings considering the proposed SST cell parameter settings. The corresponding IGBT bridge input current i_{dc1} is drawn in the third part of Fig. 4.

The average input current $\langle i_{dc1} \rangle$ is calculated by (4) from the DC input voltage V_A and the rated SST cell power. The maximum value in the input I_M in the inverter and the transformer is derived from the current wave-forms in figure 4 by (5).

$$\langle i_{dc1} \rangle = \frac{P_{out}}{v_A} \quad (4)$$

$$I_M = 2 \cdot \langle i_{dc1} \rangle \quad (5)$$

In the electronic converters, two kinds of losses must be considered: switching and conduction ones. The conduction losses are given by (6) from the saturation voltage $V_{CE(sat)}$ and the collector current mean value $\langle i_c \rangle$ calculated from the current wave-forms presented in the lower part of Fig. 4.

$$P_{cond} = V_{CE(sat)} \cdot \langle i_c \rangle \quad (6)$$

$$\langle i_c \rangle = \frac{1}{T} \int_0^T i_c dt = \frac{5}{16} I_M \quad (7)$$

The losses in the converters are calculated separately for the waveforms shown in Figure 4.

The energy W_{OFF} lost during the transistor turn-off transition is given by (8).

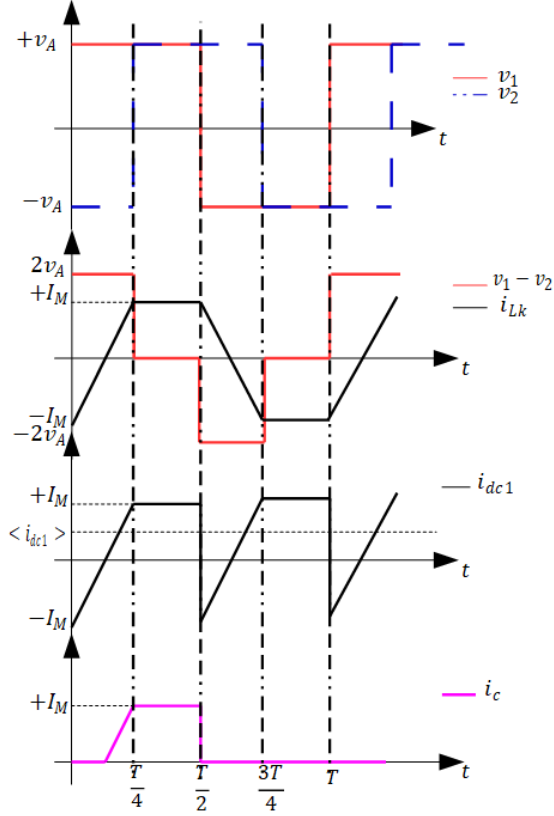


Fig. 4: Voltage and current wave-forms in the SST cell for a time lag of $\frac{T}{4}$ that corresponds to the maximum power flow.

$$W_{OFF} = \frac{1}{2} \cdot v_A \cdot I_M \cdot t_f \quad (8)$$

The same estimation can be made for the IGBTs of the second converter. The total switching losses of SST cell can be estimated by (9). Where t_f is the fall time.

$$P_{SW} = W_{OFF} \cdot f = \frac{1}{2} \cdot v_A \cdot I_M \cdot t_f \cdot f \quad (9)$$

The two converters are identical to each other, then, the respective losses are equal. Since each converter is made of four identical switches, total converter loss of SST cell is given by (10). The data-sheet of IGBTs module gives $t_f = 60ns$, $V_{CE(sat)} = 2.1V$ and diode with $V_F = 1.8V$ at $125^\circ C$ [14].

$$P_{conv} = 8 \cdot (P_{SW} + P_{cond,IGBT} + P_{cond,diode}) \quad (10)$$

C. Winding losses estimation

For medium and high frequencies, skin and proximity effects naturally increase the wire AC resistance relatively to the DC one. Several work show that the AC resistance increase is limited by using litz wires made of many elementary enamelled wires of small diameter connected in parallel. The ratio

R_{AC}/R_{DC} depends on the number of elementary enamelled wires, on their diameter on the winding topology and on the frequency [15] [16]. The manufacturers propose several products of round or rectangular litz wires designed for getting good filling factors [17]. The product choice depends on the technological choices made for the MFT design. For getting a reasonable degree of freedom for litz wire choice in the manufacturer data-sheets, the maximum ratio of R_{AC}/R_{DC} has been set to 1.4. The DC resistance values (R_{DCp} and R_{DCs}) are computed from lengths and cross section of the wire used for manufacturing the primary and secondary windings. These resistances depend on the sizing options presented in section E. The RMS currents in the MFT windings are computed from the wave-form of the middle graph of Fig. 4 applying the classical definition (11) and the copper losses derive from this current by (12).

$$I_{RMS} = \sqrt{\frac{1}{T} \int_0^T i_{LK}^2 dt} = I_M \sqrt{\frac{2}{3}} \quad (11)$$

$$P_W = (R_{ACp} + R_{ACs}) I_{RMS}^2 \quad (12)$$

D. Core losses

The manufacturing process of the core on the magnetic properties is of utmost importance as well as the influence of the voltage waveform. This is why two kinds of voltage waveform have been assessed, the classical sine and the rectangular one. Experimental investigations have been made at several frequencies and peak flux densities for determining the core losses. Fig. 5 show a wound core, which has been cut for facilitating the transformer coil assembly.



Fig. 5: Cut wound core.

For testing, two specific winding have been distributed along the core. The numbers of turns are identical ($N_2 = N_1$). The primary winding is fed by a square wave or sine wave. The steps to get the core loss are:

- Measure the $i_{LK}(t)$ current flowing through primary winding when the secondary winding in open circuit. This current is measured with a current probe, it is in direct

related with the magnetic field according to the Ampere's law $i_{LK}(t) = \frac{H(t) \cdot l_m}{N_1}$.

- Measure the voltage induced in the secondary winding $v_2(t)$; $v_2(t) = -A_c \cdot N_2 \frac{dB(t)}{dt}$.
- Calculate the average of the product $i_{LK}(t) \cdot v_2(t)$ during a period T given by (13):

$$P = \frac{1}{T} \frac{N_1}{N_2} \int_0^T i_{LK}(t) \cdot v_2(t) dt \quad (13)$$

Measurements are performed at steady state after demagnetizing the core. The primary current is measured using a non-inductive shunt with a channel of the oscilloscope and the voltage with another one. Data are stored in an oscilloscope, 10000 points for each measurement, and transferred to a PC; and a Matlab script perform the integration.

For the same peak flux density, measurement results of Fig. 6, made at 1 and 2kHz, show lower losses for square voltages than for sine ones. Similar result exists in the literature on ferrite and amorphous cores [18]. These results show that the square voltage waves obtained with simple converters using only a single switching per IGBT leg and per period can be used rather than to more complex PWM inverters able to produce voltage waves close than sine ones.

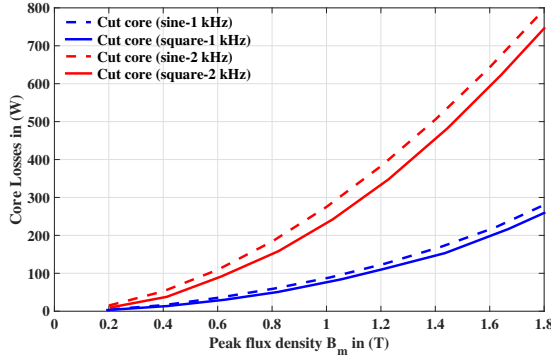


Fig. 6: Comparisons of magnetic core losses under sinusoidal and square voltages.

Fig. 7 shows core losses for square-voltage waves versus frequency for several peak flux densities.

E. SST cell global design

From sections B, C and D, the overall efficiency of SST cell, η , can be calculated by (14) for several design options.

$$\eta = \frac{P_{out}}{P_{out} + P_{conv} + P_W + P_{core}} \quad (14)$$

The design procedure of the MFT consist of several steps with two constants for getting an easy comparison:

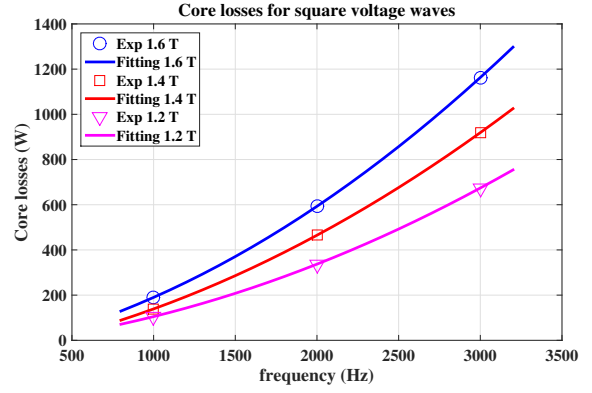


Fig. 7: Core losses as a function of frequency for several flux density peak values.

- the wound-core size presented in figure 2 (core weight = 2.9 kg).
- the copper filling ratio set to 30% for getting room for the insulation(that corresponds to a copper weight = 10.18 kg).

The other variable parameters are tuned for analyzing the design balance when the cooling system is able get temperatures compatible with the temperature electrical insulation system. Four input variables are used :

- the rated power;
- the input SST-cell voltage
- the frequency;
- the maximum flux density.

The lines of Table I are computed from the input constants and variables with the results of sections B, C and D. The turn number N of each coil is computed from the maximum flux density, the core section and the frequency. The cross section (S_{cu}) of the Litz copper wire depends on the size of the core window because the filling factor is kept constant for insulation. Consequently the current density and the copper losses depends on the input variables. The converter losses is slightly dependent on frequency and more on the current. The core losses depends strongly on the frequency. As the filling factor is kept constant, the wire section increase with frequency and the the winding losses reduce. This approach provides a global analysis on the balance of losses for three frequencies.

Table I, shows that an overall efficiency over 95% can be achieved when the cooling system keeps the temperature under the electrical insulation thermal class. Table II estimates the SST-cell performances in such cases with a higher voltage for 3kHz and two peak flux densities.

Comparing to the results of Table I, Table II show that a higher power/mass ratio is possible accepting slightly higher copper losses. For the same rated power a higher voltage reduces slightly the losses in the converter. Efficiency remains

TABLE I
DESIGN PARAMETERS OF THE SST CELL AT 1.6T

	$P = 40kW - 800V$			$P = 50kW - 800V$		
	1.5	2	3	1.5	2	3
$f(kHz)$	1.5	2	3	1.5	2	3
$N(turns)$	128	96	64	128	96	64
$S_{cu}(mm^2)$	17.5	23	35	17.5	23	35
$I_{RMS}(A)$	81.6	81.6	81.6	102	102	102
$J_{cu}(A/mm^2)$	4.65	3.49	2.35	5.8	4.3	2.9
$P_{conv}(W)$	644	653	672	804	816	840
$P_{core}(W)$	371	596	1163	371	593	1163
$P_W(W)$	847	476	211	1321	744	330
η	95.55	95.87	95.1	95.2	95.8	95.5

TABLE II
DESIGN PARAMETERS OF THE SST CELL AT 3kHz

	$P = 50kW - 1000V$			$P = 60kW - 1000V$		
	1.2	1.4	1.6	1.2	1.4	1.6
$B_m(T)$	1.2	1.4	1.6	1.2	1.4	1.6
$N(turns)$	107	92	80	107	92	80
$S_{cu}(mm^2)$	21	24.4	28.08	21	24.4	28.08
$I_{RMS}(A)$	81.6	81.6	81.6	97.97	97.9	97.9
$J_{cu}(A/mm^2)$	3.88	3.34	2.9	4.66	4.01	3.48
$P_{conv}(W)$	687	687	687	824.4	824.4	824.4
$P_{core}(W)$	674	919	1163	674	919	1163
$P_W(W)$	591.6	437.4	330.7	852	629.8	476.28
η	96.24	96.07	95.82	96.23	96.2	96.06

around 96% whatever the balance between core losses and copper losses.

These results show that it is possible to design high power SST-cells with a power/mass ratio up to $4.6kW/kg$ with wound cores made of thin GOES able to operate at high temperatures.

The next step is to define the cooling system and a thermal design able to guarantee a winding temperature compatible with the thermal class of present-day polymers that can reach $200^\circ C$ for a live span of 20000 hours.

III. DETAILS ON CONTROL STRATEGIES

A. Model of a cell within the global structure

The main concept of a modular SST based upon the association of N elementary cells is illustrated by Fig. 8. The input converters are connected in series to share the high voltage (HV) and low voltage side connects the converters in parallel for providing a high current. The control of each cell ensure the global balance of the structure.

Neglecting the magnetizing current, the transformer can be modelled by the equivalent circuit (Fig. 9) the reduces to the figure Fig. 10 for the equivalent currents and voltages seen from the primary side. R_s is the equivalent global resistance ($R_s = n^2 \cdot r_1 + r_2$) and L_K the global leakage inductance ($L_K = n^2 \cdot l_1 + l_2$).

$$R_s \cdot i_{LK} + L_K \cdot \frac{di_{LK}}{dt} = v_1 - v_2 \quad (15)$$

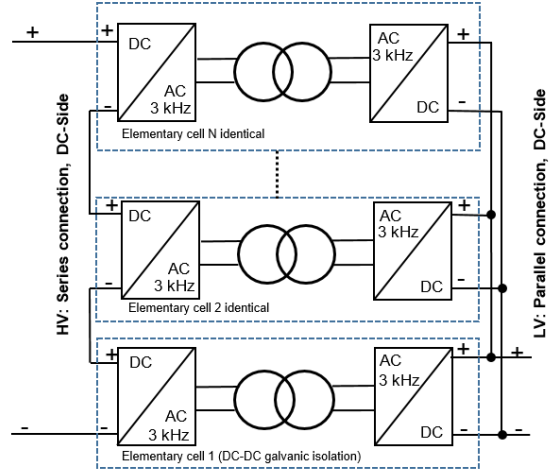


Fig. 8: Modular structure of a high power SST made with N identical cells.

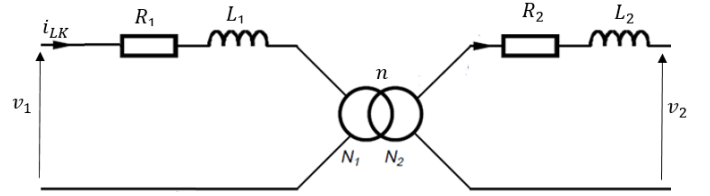


Fig. 9: Equivalent circuit of the transformer of a cell.

For handling the control of the IGBTs, the principle described by [19] has been chosen. It consists in monitoring the three control parameters defined in Table III for the case of one commutation per period as showed by Fig. 11. Each converter generates a positive, a negative and a zero voltages.

TABLE III
MODULATION PARAMETERS FOR THE DAB.

Phase shift between v_1 and v_2	ϕ
Zero-voltage width for v_1	β_1
Zero-voltage width for v_2	β_2

The operating principle depends on the phase shift ϕ introduced between the rectangular voltages generated by the two bridges. If the two voltages v_1 and v_2 are exactly the same, there will be no power transfer. However, as soon as a phase shift is introduced between them, an alternating current is generated. This current will depend on the voltage difference, as well as on the leakage inductance L_K of the transformer.

B. Different types of control and comparison

1) Phase Shift Modulation: (PSM)

The power transfer is controlled via the single parameter ϕ , with: $\beta_1 = \beta_2 = 0$ and $-\frac{\pi}{2} \leq \phi \leq \frac{\pi}{2}$. It is inversely

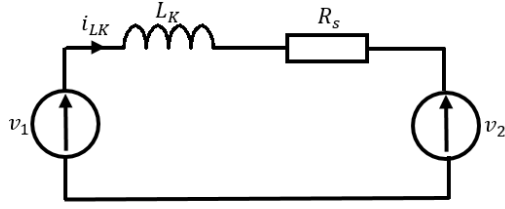


Fig. 10: Global equivalent of the SST cell circuit.

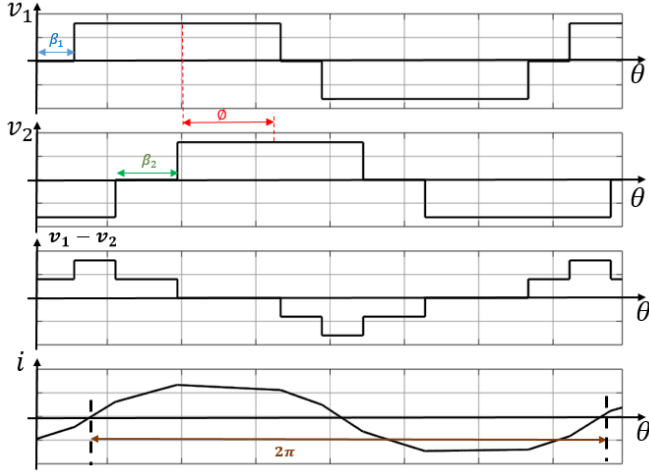


Fig. 11: Voltage and current waveforms, depending on the control parameters ϕ , β_1 and β_2 .

proportional to the leakage inductance as expressed in (16). This equation is representative of the magnitude and direction of the power flow by the value of ϕ . The maximum transmitted power is obtained for $\phi = \pm \frac{\pi}{2}$.

$$P = \frac{V_A \cdot V_B}{\omega \cdot L_K \cdot \pi} \phi \cdot (\pi - |\phi|) \quad (16)$$

2) Trapezoidal Modulation: (TZM)

Parameters β_1 , β_2 can be used to as complementary for controlling the power flow control adjustment as illustrated by Fig. 11. In this graph, the three parameters vary, for computing the transmitted power. The maximum power is found when $\phi = \frac{\pi}{2}$ and $\beta_1, \beta_2 = 0$; which corresponds to the PSM method.

3) Triangular Modulation: (TRM)

This method is a particular case of TZM. Only β_1 , β_2 are varied, keeping $\phi = 0$. Several statements arise:

- $\beta_1 = \beta_2$: The two control v_1 and v_2 voltages are identical, no current in the AC link thus no power.
- $\beta_2 \geq \beta_1$: Power flows from primary to the secondary.
- $\beta_2 \leq \beta_1$: Power flows from the secondary to the primary.

The maximum power transmitted for this method is half the one obtained with the other ones.

The phase shift modulation (PSM) and the trapezoidal modulation (TZM) show a better control strategy compared to triangular modulation (TRM), with regard to the maximum transmitted power. However, for a complex association of several SST cells (Fig. 8), the global control is complex and the other parameters β_1 and β_2 provide degrees of flexibility that may be useful.

C. Choice of a control strategy for the elementary cell

The simpler control strategy, that uses only one parameter ϕ , has been chosen for the SST cell. This PSM method is adequate to control an SST cell with a wide power transfer range. Fig. 12 presents a practical application where the SST cell supplies a DC load, which must be regulated at a constant voltage v_B whatever the load current i_{Load} .

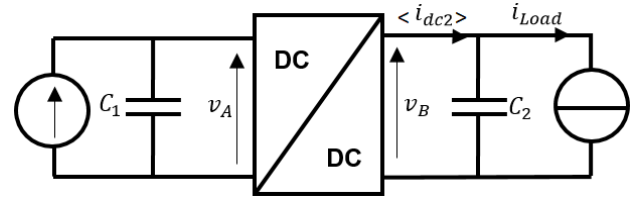


Fig. 12: The SST cell in its functional context.

The output voltage v_B is kept constant by the SST cell that acts on its internal control parameter. The control loop of Fig. 13 gives details. The controller acts on the internal parameter ϕ for regulating the output voltage v_B very near the set point value whatever could be the SST cell output current and the input voltage in the operating range of the cell.

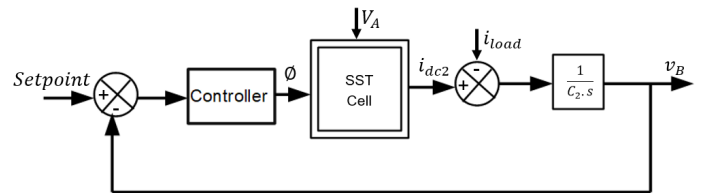


Fig. 13: The block diagram of a SST cell.

The output voltage v_B depends on the output capacitance and currents. Assuming that the capacitance C_2 has a large value, v_B is suppose to remain constant during short times. Consequently the instantaneous value for the control loop can be assimilated to the mean value of the voltage defined at the short time scale of the power electronic converters ($v_B \approx \langle v_B \rangle$). The output power is expressed by (18) and the output current mean value by (19).

$$v_B = \frac{1}{C_2} \int (\langle i_{dc2} \rangle - i_{Load}) dt \quad (17)$$

$$P_2 = \langle v_B \rangle \cdot \langle i_{dc2} \rangle \quad (18)$$

$$\langle i_{dc2} \rangle = \frac{V_A}{\omega \cdot L_K \cdot \pi} \phi \cdot (\pi - \phi) \quad (19)$$

The controller of Fig. 13 must be tuned for providing the the loop stability and the required voltage accuracy of the SST cell.

IV. DISCUSSIONS ON THE RELIABILITY OF THE PROPOSES SST CELLS

The main goal of the paper consist in opening the possibility of designing large power elementary SSTs cells, in the range of $1MW$, for building large power SSTs by assembling these elementary cells. For such high power systems, the structural reliability is a key point. The option is to base the design on mature technologies (TRL8 or TRL9) [20].

The structural reliability of the SST cell depends on the one of the subsystems (Inverter and transformer) and on the quality of their assembly:

- The inverters operate in kHz range frequency with Silicon IGBTs and simple commands (two switching per period).
- The medium frequency transformer designed with a hot wound core made of thin GOES laminations and coils made of standard Class 200°C enamelled wire.
- The mechanical and electrical assembly of components uses mature methods used for a long time in power electronic industry.

A. Inverter structural reliability

Generally speaking, the lifetime of Si-IGBT modules depends mainly on electrical and thermal stresses. The reliability relative to the electrical stress is obtained, using a correct safety controlled with a correct safety margin for the module rated voltage and low inductance connections (laminated busbars and low parasitic inductance decoupling capacitors placed at the strategic position of the laminated busbar).

The Si-IGBTs structural reliability relative to the thermal stress has been studied for a long time [21]. It is now well known that IGBT module can work for limited lifetimes over the rated chip temperature [22]; with the proposed simple command, the IGBT losses are limited and the cooling system can be designed for limiting the IGBT chips under the rated temperature for increasing the expected lifespan.

The structural reliability of IGBT modules depends mainly of the mechanical stress on the bonding and on the packaging due to thermal cycles [23]. This study is made with short thermal cycles for pratical experiments reasons, but it can be extended to long cycles. Figure 14 extracted from [23] gives an example of results for $10s$ thermal cycles and a end-of life

criterion define as an increase of the Collector-Emitter saturation voltage. This study shows that the sample lifespan is over 10000 cycles.

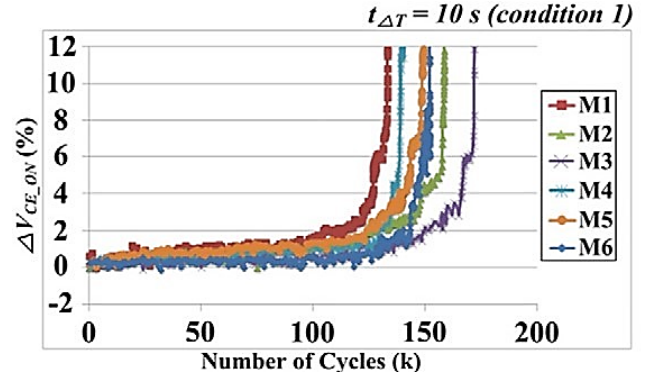


Fig. 14: Example of thermal cycling tests of IGBT modules. The end-of life criteria is the unacceptable increase of the on voltage [23].

B. MFT structural reliability

The important parameter is the thermal class of the winding wire; it is defined by the IEC 60216-3 standard [24] as the maximum temperature for a lifetime of $20000h$ with a failure rate of 50% for an applied voltage of $1000V$ during $1min$. This standard uses Arrhenius' law for predicting the lifetime of a coil. The IEC 60172 standard [25] allows the Arrhenius curve to be drawn for enamelled wire of class 200°C often used for electric machine windings, a lifetime of 200000 hours can be achieved by working at a lower temperature (155°C) according the Arrhenius law (figure 15).

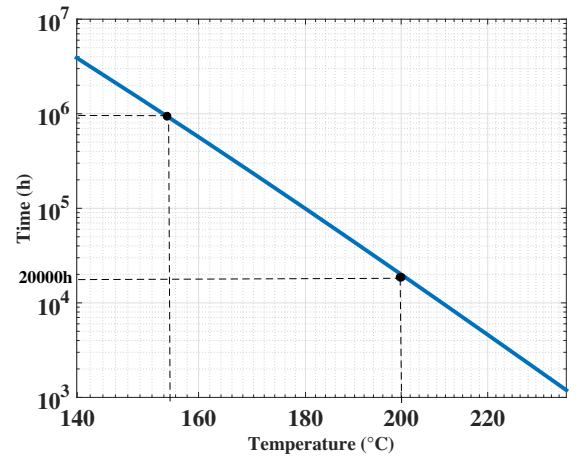


Fig. 15: Arrhenius curve for thermal class 200°C winding wire [25].

The hot GOES wound core is also an element of the SST cell structural reliability. The natural insulation layer of GOES products is made of an inorganic magnesium silicate film (glass

film) on which has been deposited a second film composed of inorganic components based on phosphates and silicates [26]. This Insulation configuration is said EC-5 on EC-2 according to the IEC 60404-1-1 standard [27]. GOES withstands sheet annealing at 850 °C. This layer is extremely stable at the expected operating temperatures of the SST cell.

MFT cooling is a key point of its structural reliability. The GOES wound core can operate at high temperature for getting a good power/mass ratio, but the winding temperature must remain under its thermal class. Consequently, a thermal insulation must be placed between the core and the winding.

V. CONCLUSION

The proposed assessments on high-power SST cells based on wound cores made of thin sheets of high performance grain-oriented electrical steel show that high power/mass ratio can be reached with a correct global efficiency at medium frequencies and high flux densities. The characterization measurements show that the magnetic core losses in square voltage excitation are lower than in sine one for the same maximum flux density and frequency. Such voltage waveforms require simple converters that can be easily transposed to very high power SST cells.

The lifetime of high power IGBTs and winding wires is a necessary element to increase confidence in the design of SST cell high power. The next step consists to define a specific thermal management of the medium frequency transformer that guarantees a winding temperature compatible with its insulation system class with a wound core that is not practically limited in temperature.

ACKNOWLEDGMENT

This work is funded by ThyssenKrupp Electrical Steel.

REFERENCES

- [1] Y. Jianyang, M. Q. Khan, Z. Yanwen, M. M. Khan, and M. Ali, "Hvdc bidirectional power flow using solid state transformer," in *Circuits, Devices and Systems (ICCDs), 2017 International Conference on*. IEEE, 2017, pp. 110–114.
- [2] T. Yao, I. Leonard, R. Ayyanar, and K. Tsakalis, "Mu synthesized robust controller for multi-sst islanded smart grid," in *Energy Conversion Congress and Exposition (ECCE), 2016 IEEE*. IEEE, 2016, pp. 1–8.
- [3] C. Zhao, D. Dujic, A. Mester, J. K. Steinke, M. Weiss, S. Lewdeni-Schmid, T. Chaudhuri, and P. Stefanutti, "Power electronic traction transformer—medium voltage prototype," *IEEE Transactions on Industrial Electronics*, vol. 61, no. 7, pp. 3257–3268, 2014.
- [4] D. Dujic, F. Kieferndorf, F. Canales, and U. Drogenik, "Power electronic traction transformer technology," in *Power Electronics and Motion Control Conference (IPEMC), 2012 7th International*, vol. 1. IEEE, 2012, pp. 636–642.
- [5] B. Zhao, Q. Song, and W. Liu, "A practical solution of high-frequency-link bidirectional solid-state transformer based on advanced components in hybrid microgrid," *IEEE Transactions on Industrial Electronics*, vol. 62, no. 7, pp. 4587–4597, 2015.
- [6] S. B. Y. Du, G. Wang, and S. Bhattacharya, "Design considerations of high voltage and high frequency transformer for solid state transformer application," in *IECON 2010-36th Annual Conference on IEEE Industrial Electronics Society*. IEEE, 2010, pp. 421–426.
- [7] F. Iturritz and P. Ladoux, "Phase-controlled multilevel converters based on dual structure associations," *IEEE Transactions on Power Electronics*, vol. 15, no. 1, pp. 92–102, 2000.
- [8] D. S. Oliveira, D. de A Honorio, L. H. S. Barreto, P. P. Praca, A. Kunzea, and S. Carvalho, "A two-stage ac/dc sst based on modular multilevel converter feasible to ac railway systems," in *Applied Power Electronics Conference and Exposition (APEC), 2014 Twenty-Ninth Annual IEEE*. IEEE, 2014, pp. 1894–1901.
- [9] P. C. Kjaer, S. Norrga, and S. Ostlund, "A primary-switched line-side converter using zero-voltage switching," *IEEE transactions on industry applications*, vol. 37, no. 6, pp. 1824–1831, 2001.
- [10] I. Villar, U. Viscarret, I. Etxeberria-Otadui, and A. Rufer, "Global loss evaluation methods for nonsinusoidally fed medium-frequency power transformers," *IEEE Transactions on Industrial Electronics*, vol. 56, no. 10, pp. 4132–4140, 2009.
- [11] D. Aguglia and M. Neuhaus, "Laminated magnetic materials losses analysis under non-sinusoidal flux waveforms in power electronics systems," in *Power Electronics and Applications (EPE), 2013 15th European Conference on*. IEEE, 2013, pp. 1–8.
- [12] B. MULTON and E. d. C.-A. de Bretagne, "Composants passifs (magnétiques et capacitifs) de l'électronique de puissance," *ENS Cachan, disponible en ligne: http://www.geea.org/IMG/pdf/ComposantsPassifs_Multon.pdf*, 2006.
- [13] V. Basso, G. Bertotti, O. Bottauscio, F. Fiorillo, M. Pasquale, M. Chiampi, and M. Repetto, "Power losses in magnetic laminations with hysteresis: Finite element modeling and experimental validation," *Journal of applied physics*, vol. 81, no. 8, pp. 5606–5608, 1997.
- [14] <https://datasheetspdf.com/datasheet/SKM400GB128D.html>.
- [15] C. R. Sullivan, "Cost-constrained selection of strand diameter and number in a litz-wire transformer winding," *IEEE Transactions on Power Electronics*, vol. 16, no. 2, pp. 281–288, 2001.
- [16] R. Wojda and M. Kazimierczuk, "Winding resistance of litz-wire and multi-strand inductors," *IET Power Electronics*, vol. 5, no. 2, pp. 257–268, 2012.
- [17] vonroll, "Winding wires and litz wires," <https://www.vonroll.com>.
- [18] D. Chen, "Comparisons of high frequency magnetic core losses under two different driving conditions: A sinusoidal voltage and a square-wave voltage," in *Power Electronics Specialists Conference, 1978 IEEE*. IEEE, 1978, pp. 237–241.
- [19] B.-J. Byen, K.-P. Kang, Y. Cho, and A. Yoo, "A high-efficiency variable modulation strategy for a dual-active-bridge converter with a wide operating range," in *Power Electronics and ECCE Asia (ICPE-ECCE Asia), 2015 9th International Conference on*. IEEE, 2015, pp. 240–245.
- [20] E. Herr and S. Dewar, "Lopak igbt modules—inverter reliability benefits," *Proc. PCIM'00, Boston, USA*, 2000.
- [21] J. Onuki, M. Koizumi, and M. Suwa, "Reliability of thick al wire bonds in igbt modules for traction motor drives," *IEEE Transactions on Advanced Packaging*, vol. 23, no. 1, pp. 108–112, 2000.
- [22] G. K. Morris, M. G. Phillips, L. Wei, and R. A. Lukaszewski, "Operating igbts above rated junction temperature limits: Impacts to reliability and electrical performance," in *2016 Annual Reliability and Maintainability Symposium (RAMS)*. IEEE, 2016, pp. 1–7.
- [23] U.-M. Choi, F. Blaabjerg, S. Jørgensen, F. Iannuzzo, H. Wang, C. Uhrenfeldt, and S. Munk-Nielsen, "Power cycling test and failure analysis of molded intelligent power igbt module under different temperature swing durations," *Microelectronics Reliability*, vol. 64, pp. 403–408, 2016.
- [24] C. 60216-3, "Détermination des propriétés d'endurance thermique des matériaux isolants électriques, cei std."
- [25] N. E. 60172, "Méthode d'essai pour la détermination de l'indice de température des fils de bobinage émaillés, cei std," 1995.
- [26] R. Lemaître and T. Belgrand, "Matériaux magnétiques doux cristallins, acier électrique à grains orientés," *Techniques de l'ingénieur*, 2014.
- [27] "Magnetic materials—part 1-1: Classification—surface insulations of electrical steel sheet, strip and laminations, iec standard 60404-1-1," 2004.